OPTICA

Experimental demonstration of continuous-variable measurement-device-independent quantum key distribution over optical fiber

Yan Tian,[1,2] Pu Wang,[1,2] Jianqiang Liu,[1,2] Shanna Du,[1,2] Wenyuan Liu,[1,2] Zhenguo Lu,[1,2] Xuyang Wang,[1,2] and Yongmin Li[1,2,*]

[1]State Key Laboratory of Quantum Optics and Quantum Optics Devices, Institute of Opto-Electronics, Shanxi University, Taiyuan, 030006, China
[2]Collaborative Innovation Center of Extreme Optics, Shanxi University, Taiyuan, 030006, China
*Corresponding author: yongmin@sxu.edu.cn

Received 7 December 2021; revised 23 March 2022; accepted 29 March 2022; published 29 April 2022

Measurement-device-independent quantum key distribution (MDI-QKD) can remove all side-channel attacks on detectors. In the context of the dramatic progress of discrete-variable MDI-QKD and twin-field QKD, owing to the critical challenge of continuous-variable (CV) Bell-state measurement (BSM) of two remote independent quantum states, experimental demonstration of CV-MDI-QKD over optical fiber has remained elusive. To solve this problem, a technology for CV-BSM of remote independent quantum states is developed that consists of optical phase locking, phase estimation, real-time phase feedback, and quadrature remapping in the present work. With this technology, CV-BSM is accurately implemented, and the first CV-MDI-QKD over optical fiber is demonstrated, to our knowledge. The achieved secret key rates are 0.43 (0.19) bits per pulse over a 5-km (10-km) optical fiber. Our work shows that it is feasible to build a CV-MDI-QKD system over optical fiber. Further, the results pave the way towards realization of a high secret key rate and low-cost metropolitan MDI-QKD network, and serve as a stepping stone to a CV quantum repeater.

https://doi.org/10.1364/OPTICA.450573

1. INTRODUCTION

Quantum key distribution (QKD) can generate information-theoretical secure keys between two parties over an insecure quantum channel, in which the security of the shared keys is guaranteed by the fundamental laws of quantum mechanics [1–5]. However, in practice, the gap between idealized models and realistic devices for QKD implementations opens various security loopholes [6] that result in a variety of targeted attacks.

Inspired by the idea of entanglement swapping, measurement-device-independent QKD (MDI-QKD) has been proposed [7,8], in which an untrusted third party, Charlie, is introduced to couple the quantum signals sent by Alice and Bob and implement Bell-state measurement (BSM). MDI-QKD can naturally remove all side-channel attacks on the measurement apparatus, which arguably comprise the most critical security loophole in QKD implementations.

Continuous-variable (CV) QKD protocols [9–12] encode the key information on quadratures of quantized light fields, which are measured by low-cost and high-efficiency balanced homodyne detectors (BHDs) instead of dedicated single-photon detectors (SPDs). The high-speed coherent detection technology and infinite-dimensional Hilbert space of the encoding promise potential higher secret key rates over a metropolitan area [13]. Moreover, because of the spatial and temporal filtering of the local-oscillator (LO) field, CV-QKD is robust against noise photons in various quantum channels [14–16].

Similar to discrete-variable (DV) QKD, CV-QKD also suffers from detection side-channel attacks, e.g., wavelength [17,18], calibration [19], and saturation attacks [20]. In contrast to the remarkable development of DV-MDI-QKD [21–31] and twin-field QKD [32–39], only a proof-of-principle demonstration of CV-MDI-QKD has been reported [40], despite CV-MDI-QKD making significant progress in theory [40–49]. Furthermore, this demonstration utilizes only one laser source for both parties, which is unsuitable for realistic MDI-QKD scenarios in which Alice and Bob are far from each other. On the other hand, this experiment exploited two short and lossless free-space quantum channels, and the losses in the links were simulated by attenuating the variances of the modulation signals. At present, a full experimental demonstration of CV-MDI-QKD over long-distance telecom single-mode optical fiber is still missing.

Two key issues make the experimental demonstration of CV-MDI-QKD over long-distance fiber challenging. The first is how to faithfully establish a reliable phase reference between two spatially separated lasers and achieve CV-BSM. Notice that CV-BSM not only requires single-photon-level interference of two remote independent lasers, but also demands dual-homodyne detection, in which simultaneous measurement of a pair of conjugate quadratures is performed. In this case, precise control of the relative phase

between the signal and LO for dual-homodyne detection should be ensured.

Another challenge arises from the untrusted and imperfect BHDs at Charlie's site. Note that the imperfect quantum efficiency of BHDs is equivalent to optical losses that inevitably induce vacuum fluctuation noises, which, along with detector electronic noises, both contribute to detection noises. These noises can be fully controlled and exploited by Eve to mask her attacks. Hence, the performance of CV-MDI-QKD heavily depends on the detection efficiency of BHDs.

In this paper, we demonstrate the first experimental CV-MDI-QKD over 10 km of telecom single-mode fiber (SMF) with high-efficiency free-space BHDs. To this end, a systematic approach for various phase-reference establishments required by CV-BSM between two remote independent quantum states is proposed and implemented that consists of optical phase locking, phase estimation, real-time phase feedback, and quadrature remapping. Furthermore, a free-space time-domain BHD with a quantum efficiency of 99% was developed. The peak value of each output electric pulse of the time-domain BHD yields a single value of the signal field quadrature, which significantly simplifies the subsequent data-acquisition procedure.

2. PROTOCOL AND SYSTEM

The preparation and measurement scheme of the CV-MDI-QKD protocol is briefly described as follows.

Step 1. Alice and Bob randomly and independently prepare their Gaussian-modulated coherent states, $|X_A + iP_A\rangle$, $|X_B + iP_B\rangle$, with variance V_A, V_B. Subsequently, Alice and Bob send their coherent states to Charlie through independent quantum channels.

Step 2. Charlie couples the received signal states of Alice and Bob at a 50:50 beam splitter (BS). Then Charlie uses two BHDs to measure the amplitude quadrature X_C and phase quadrature P_C of the output modes. The measurement outcomes for an ideal CV-BSM are $X_C = (1/\sqrt{2})(X_A - X_B)$ and $P_C = (1/\sqrt{2})(P_A + P_B)$. After the data transmission phase is completed, Charlie announces his measurement results: $r = (X_C + iP_C)/\sqrt{2}$.

Step 3. Based on the measurement results published by Charlie, Alice and Bob displace their respective raw data as $X_{dA} = X_A - g_{X_A}(r)$, $P_{dA} = P_A - g_{P_A}(r)$ and $X_{dB} = X_B - g_{X_B}(r)$, $P_{dB} = P_B - g_{P_B}(r)$. g_*, $* = X_A$, P_A, X_B, P_B, is the displacement function (see Supplement 1 for details).

Step 4. Alice and Bob perform parameter estimation, data reconciliation, and privacy amplification through an authenticated public channel to generate the final secret key.

In our experimental realization, we implement the Gaussian-modulated coherent-state CV-MDI-QKD scheme. A schematic of the experimental setup is illustrated in Fig. 1. Alice exploits a single-frequency continuous-wave (cw) 1550-nm laser with a linewidth of approximately 2 kHz. Two cascaded amplitude modulators (AM1 and AM2), are used to generate 50-ns light pulses at a repetition rate of 500 kHz. The light pulses are split into signal and phase-reference pulses by a 1:99 BS. AM3 and a phase modulator (PM) are adopted to modulate the signal field randomly with zero-centered Gaussian distributions in phase space. A combination of a polarizing BS (PBS), SMF, and Faraday mirror (FM) is employed to delay signal pulses by 300 ns to realize time-multiplexing. A variable optical attenuator (VOA) further attenuates the intensity of the signal pulses to a suitable level. Finally, the signal and phase-reference fields are polarization-multiplexed via a PBS and transmitted through a SMF-28 fiber spool to Charlie. A portion of Alice's laser is sent to Bob and interferes with Bob's laser, the resulting interference signal is fed into an optical phase-locked loop (OPLL) to stabilize the relative phase between Alice's and Bob's lasers.

At Bob's site, a single-frequency cw laser with a linewidth of 4 kHz is employed, and operations similar to Alice's are performed. Instead of generating the signal and phase-reference fields, Bob prepares the signal and LO fields.

At Charlie's site, the signal and LO (reference) beams are polarization-de-multiplexed via a PBS and then temporally aligned

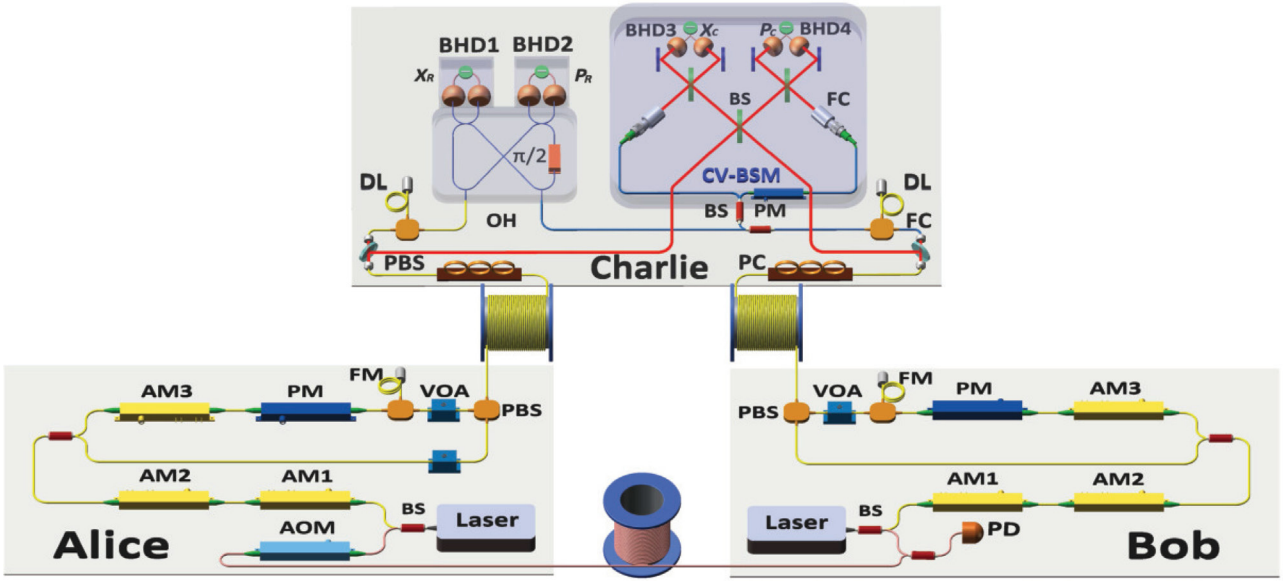

Fig. 1. CV-MDI-QKD setup. BS, beam splitter; AM, amplitude modulator; AOM, acousto-optic modulator; PM, phase modulator; FM, Faraday mirror; VOA, variable optical attenuator; PBS, polarizing beam splitter; PD, photodetector; PC, polarization controller; FC, fiber collimator; DL, delay line; OH, optical hybrid; BHD, balanced homodyne detector.

with delay lines. A portion of the LO pulses interferes with the phase-reference pulses in a 90-deg optical hybrid, and the output light beams are fed into two time-domain BHDs. To achieve high-efficiency CV-BSM, the signal and LO fields are coupled from optical fibers to free space, and the CV-BSM are implemented with free-space bulk components that have negligible losses. Two time-domain BHDs with a quantum efficiency of 99% are developed to measure two conjugated quadratures. Considering the insertion loss of the optical components and visibility of interference fringes, the entire detection efficiency is 97.2% (see Supplement 1 for details). The PM located on one of the LO paths is used to compensate for the slow phase drift for two conjugated quadratures measurement.

In our proof-of-principle experiment, we directly synchronize the state generation of Alice and Bob through an electrical synchronization method. More precisely, at Alice's (Bob's) site, two parallel pulse generators that can adjust the pulse width and clock signal delay are used to generate 50-ns electrical pulse signals at a repetition rate of 500 kHz to drive AM1 and AM2. Then, two clock signals from the same signal source are input into the pulse generators of Alice and Bob to ensure that Alice and Bob generate pulse signals synchronously. At Charlie's site, a portion of LO pulses after polarization-de-multiplexing is used for clock recovery (see Appendix C for details).

3. RESULTS AND DISCUSSION

The key challenge for CV-MDI-QKD is to achieve CV-BSM of two independent quantum states at Charlie's station, which requires precise control of the relative phase between the signal and LO. The phase-reference benchmarks for Gaussian modulation of Alice and Bob are the phases of the reference and LO pulse, respectively. At Charlie's site, the LO field for CV-BSM comes from Bob's laser. Therefore, there exists only slow phase drift between Bob's signal and LO pulses when they arrive at Charlie's station. The slow phase drift has a typical fluctuation rate of Hertz level, which comes from the asymmetrical Mach–Zehnder interferometers (AMZIs) employed in time-multiplexing. However, the relative phase between Alice's signal and LO pulses at Charlie's station includes both the slow phase drift due to the AMZIs and the fast phase shift. The fast phase shift is caused by the frequency difference between Alice's and Bob's lasers operating in free-running mode, the phase noise associated with the finite laser linewidth, and the optical fiber path difference from Alice (Bob) to Charlie [34,50,51] (see Appendix A for details).

A. Estimating of Fast Phase Shift

To this end, precise control of the relative phase between independent lasers should be established first. Different from twin-field (TF) QKD (TFQKD) in [39] where the relative phase estimation is implemented using reference pulses in 10 basic periods (10 μs), we measured the fast phase shift for each optical pulse by a 90-deg optical hybrid. Therefore, we need only to ensure that the relative phase of the independent lasers remains unchanged during the duration of a single light pulse. Within the duration of a single light pulse, the phase difference between Alice's and Bob's independent lasers is given by [50] $\Delta\theta_0 = 2\pi(f_A - f_B)\cdot T_d + 2\pi(\Delta f_A + \Delta f_B)\cdot T_d$, where $f_A(f_B)$ and $\Delta f_A(\Delta f_B)$ are the center frequency and linewidth, respectively, of Alice's (Bob's) laser, and T_d is the duration of the light pulse. In our proof-of-concept experimental demonstration, to ensure that $\Delta\theta$ remains constant (less than 1 deg) during the pulse duration of $T_d = 50$ ns to get sufficiently low excess noise, the frequency difference of the two lasers should be less than 50 kHz. To this end, an OPLL is adopted to achieve the above requirements. The locking performance can be found in Supplement 1.

To estimate the fast phase shift and establish an identical phase reference for Alice and Bob, Alice (Bob) sends out both signal pulses and phase-reference (LO) pulses that stem from the same pulses and have an identical optical phase. The average photon number per reference pulse is set to approximately 10^4 [50] to suppress the influence of shot noise and ensure accurate phase estimation. Then, Charlie performs heterodyne detection and obtains the amplitude quadrature X_R and phase quadrature P_R of the phase-reference pulses with a 90-deg optical hybrid. In this way, the fast phase shift for each signal pulse can be estimated by

$$\Delta\theta = \tan^{-1}\left(\frac{P_R}{X_R}\right). \tag{1}$$

B. Estimating of Slow Phase Drifts

We denote the slow phase drifts between Alice's signal and LO (Bob's signal and LO) in dual-homodyne detection as φ_A^X and φ_A^P (φ_B^X and φ_B^P), respectively. To accurately estimate the slow phase drifts in real time, Alice and Bob periodically insert some phase-calibration pulses into the signal pulses [52], different from phase-reference pulses, which are intense and can provide an accurate fast phase shift estimation by measuring only a single pulse. Each phase-calibration pulse possesses roughly 90 photons and therefore suffers from shot noise. To eliminate the impact of shot noise, a large number of measurement results of phase-calibration pulses are averaged within a frame time $\Delta T = 10$ ms. Note that the slow phase drift is slow enough that it can be considered a constant within a frame time. In our experiment, there are a total of 400 phase-calibration pulses of the same type for Bob in one frame. However, this averaging method is not suitable for Alice, because the measurement results of each phase-calibration pulse are completely different due to a random fast phase shift experienced by each pulse. Here, it is proposed to apply probability statistics to the measurement results to accurately estimate Alice's slow phase drift (see Appendix B for details).

C. CV-BSM

By employing the above methods, fast and slow phase drifts can be estimated in real time. The next challenge to implement CV-BSM requires simultaneous measurements of a pair of conjugated quadratures $X_C = (1/\sqrt{2})(X_A - X_B)$ and $P_C = (1/\sqrt{2})(P_A + P_B)$, where $X_A(X_B)$ and $P_A(P_B)$ are the amplitude and phase quadratures, respectively, of Alice's (Bob's) signal mode. To handle this issue, a method is proposed herein that combines real-time phase-feedback control with a quadrature remapping scheme.

Owing to the symmetry of the optical paths of CV-BSM, the difference of the slow phase drift of Alice, $\Delta\varphi_A = \varphi_A^P - \varphi_A^X$, is exactly equal to that of Bob, $\Delta\varphi_B = \varphi_B^P - \varphi_B^X$. Therefore, based on the values of φ_A^X, φ_A^P, φ_B^X, and φ_B^P estimated by the phase-calibration pulses of Alice and Bob in real time, Charlie can apply

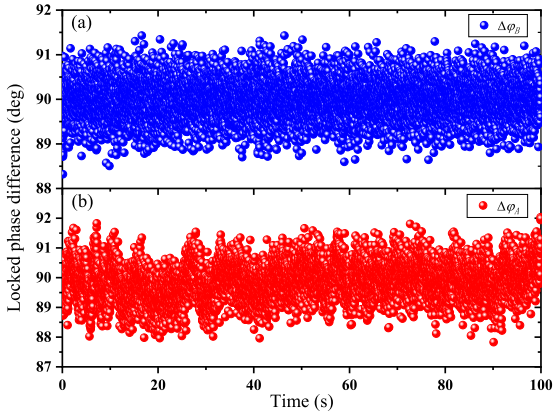

Fig. 2. (a) Locked phase difference of quadratures measured by BHD3 and BHD4 within 100 s. Mean value and standard deviation of the quadrature phase difference are 89.99° and 0.41°, respectively. (b) Phase difference $\Delta\varphi_A$ estimated by Alice's phase-calibration pulses. The mean value and standard deviation are 89.88° and 0.59°, respectively. Each data point is obtained in a frame time of 10 ms.

a compensated phase shift $\varphi_{\mathrm{PM}}^{\mathrm{LO}}$ to one of the LO fields in CV-BSM by using a PM, so that the field quadratures measured by dual-homodyne detection are faithfully orthogonal:

$$\varphi_A^P - \varphi_A^X + \varphi_{\mathrm{PM}}^{\mathrm{LO}} = \varphi_B^P - \varphi_B^X + \varphi_{\mathrm{PM}}^{\mathrm{LO}} = \frac{\pi}{2}. \tag{2}$$

In the experiment, we use $\varphi_{\mathrm{PM}}^{\mathrm{LO}} = \pi/2 - \Delta\varphi_B$ as the feedback signal, and the corresponding modulation voltage is applied to the PM. Figure 2(a) shows the locked phase difference of the quadratures $\Delta\varphi_B$ measured by Charlie within 100 s. Figure 2(b) depicts the locked phase difference $\Delta\varphi_A$ estimated by Alice's phase-calibration pulses. It can be seen that both $\Delta\varphi_B$ and $\Delta\varphi_A$ are stabilized at 90 deg at all times, which verifies the validity of Eq. (2) and the accuracy of Alice's estimating method for slow phase drift.

The above quadrature phase locking ensures only that the quadratures measured by the dual-homodyne detectors are always conjugated to each other. However, the quadrature phases are not fixed in phase space; instead, they fluctuate randomly. This will cause the data measured by Charlie to be mismatched with the data of Alice and Bob. To overcome this issue, a quadrature remapping scheme is utilized. After Charlie performs his measurement, he declares the estimated phase drifts $\Delta\theta, \varphi_A^X$, and φ_B^X publicly. Then, both Alice and Bob rotate their data at hand with the estimated phase-drift information:

$$\begin{pmatrix} X_A' \\ P_A' \end{pmatrix} = \begin{pmatrix} \cos\left(\Delta\theta + \varphi_A^X\right) & \sin\left(\Delta\theta + \varphi_A^X\right) \\ -\sin\left(\Delta\theta + \varphi_A^X\right) & \cos\left(\Delta\theta + \varphi_A^X\right) \end{pmatrix} \begin{pmatrix} X_A \\ P_A \end{pmatrix},$$

$$\begin{pmatrix} X_B' \\ P_B' \end{pmatrix} = \begin{pmatrix} \cos\left(\varphi_B^X\right) & \sin\left(\varphi_B^X\right) \\ -\sin\left(\varphi_B^X\right) & \cos\left(\varphi_B^X\right) \end{pmatrix} \begin{pmatrix} X_B \\ P_B \end{pmatrix}, \tag{3}$$

where X_A', $P_A'(X_B', P_B')$ are a pair of conjugated quadratures of Alice's (Bob's) signal mode after quadrature remapping. The rotated quadratures of Alice and Bob completely match the requirements of CV-BSM at Charlie's side:

$$X_C' = \frac{1}{\sqrt{2}}(X_A' - X_B'),$$

$$P_C' = \frac{1}{\sqrt{2}}(P_A' + P_B'), \tag{4}$$

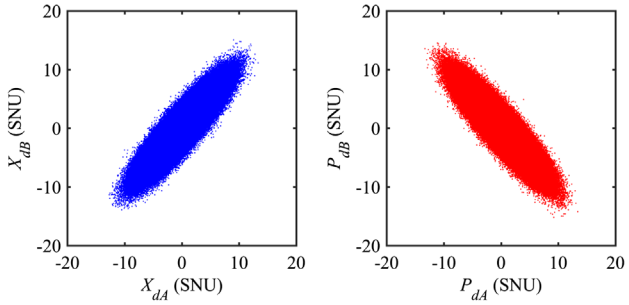

Fig. 3. Correlations of the normalized quadratures of Alice and Bob after displacement operations.

where $X_C'(P_C')$ are Charlie's BSM outcomes after quadrature phase locking. For simplicity, ideal quantum channels and BHDs are assumed here (see Supplement 1 for details).

D. Displacement Operations

Since Alice and Bob locally prepare their coherent states, the complex amplitudes of which are independently and identically distributed, the data between Alice and Bob are not correlated. To extract the secret key, Alice and Bob perform displacement operations on their own data according to Charlie's measurement results $r = (X_C' + iP_C')/\sqrt{2}$ to correlate their data [53] (see Supplement 1 for details). Figure 3 shows the correlations of the normalized quadratures of Alice and Bob after displacement operations.

E. Secret Key

Then, Alice and Bob estimate the covariance matrix and successively calculate the asymptotic secret key rate against collective attacks by [40] (see Supplement 1 for details)

$$K = \beta \cdot I_{AB|r} - \chi_{BE|r}, \tag{5}$$

where r stands for the outcome of relay, $I_{AB|r}$ is the Shannon mutual information between Alice and Bob, $\chi_{BE|r}$ is the Holevo bound between Bob and Eve, and β is the reconciliation efficiency. Here, it is assumed that Bob is the encoder and Alice the decoder.

We implement the CV-MDI-QKD scheme over different lengths of standard telecom optical fiber. Note that the modulation noise plays a key role in the excess noise ε of the system, and it is proportional to the modulation variance. However, it is found that the improvement of the secret key rate is not evident when the modulation variances V_A (Alice) and V_B (Bob) are higher than 20 N_0, where N_0 is the shot-noise unit. Therefore, to suppress the excess noise, the modulation variance of Alice and Bob is set to 20 N_0 and not optimized. For each channel length, the QKD system is operated over 1 h of acquisition time. A total number of $N = 200$ M signal pulses are sent out and measured for extraction of the secret key.

The experimental results and numerical simulations for secret key rates are illustrated in Fig. 4. Table 1 lists the relevant parameters used to theoretically estimate the secure key rate, where v_e and η are the electrical noise and detection efficiency of homodyne detectors, respectively. Note that the excess noise ε is the total excess noise of the receiver, Charlie (see Supplement 1 for details). The red dashed-dotted curve and blue solid curve in the figure denote the numerical simulations when the distance between Bob

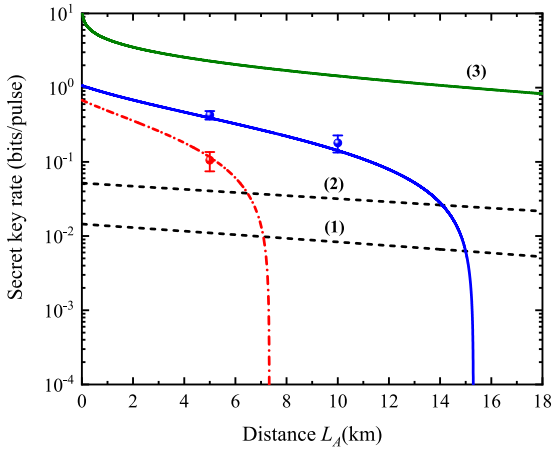

Fig. 4. Secret key rates versus L_A with different L_B of 1.06 and 0.1 km. Red dot shows experimental result at $L_B = 1.06$ km and $L_A = 5$ km, while red dashed-dotted curve denotes simulation result. Blue dots show experimental results at $L_B = 0.1$ km and $L_A = 5$ and 10 km, and blue solid curve denotes simulation result. For comparison, secret key rates of DV-MDI-QKD with optimal APD single-photon detectors (1) and cryogenic single-photon detectors (2) are also plotted. The green solid curve (3) denotes the PLOB bound.

Table 1. Parameters Used to Estimate Secure Key Rate

α	β	v_e	η	V_A	V_B	ε
0.2 dB/km	0.97	0.01	0.972	$20N_0$	$20N_0$	$0.005N_0$

and Charlie are $L_B = 1.06$ km and $L_B = 0.1$ km, respectively. The three dots correspond to the experimental secret key rates at different fiber transmission distances: (i) the distance between Bob and Charlie is $L_B = 1.06$ km, while that between Alice and Charlie is $L_A = 5$ km, and the resulting secret key rate is 0.10 bits/pulse. (ii) $L_B = 0.1$ km and $L_A = 5$ and 10 km. The corresponding secret key rates are 0.43 and 0.19 bits/pulse, respectively. For comparison, the secret key rates of DV-MDI-QKD with optimal avalanche photodiode (APD) SPDs (cryogenic SPDs) are also shown in Fig. 4 [54]. The parameters used for the secret-key-rate estimation are $\eta \sim 55\%$, $Y_0 \sim 5 \times 10^{-4}$, $e_d \sim 0.1\%$, and $f_e = 1.16$ ($\eta \sim 93\%$, $Y_0 \sim 10^{-6}$, $e_d \sim 0.1\%$, and $f_e = 1.16$), where η and Y_0 are the detection efficiency and dark count rate of SPD, e_d is the intrinsic error rate, and f_e is the error correction efficiency parameter. Finally, the green solid curve illustrates the Pirandola–Laurenza–Ottaviani–Banchi (PLOB) bound [13]. When the transmission distance is less than 15 km, it is evident that the secret key rate of the CV protocol is significantly better than that of its DV counterpart even considering the ideal cryogenic detectors. The experimental results of excess noises can be found in Supplement 1.

4. CONCLUSION

In conclusion, a set of technologies consisting of phase locking, phase estimation, real-time phase feedback, and quadrature remapping has been developed, which have the characteristics of easy implementation and application, and high compensation accuracy. With these technologies, CV BSM of two remote independent quantum states was achieved, and the first experimental demonstration of CV-MDI-QKD over 10 km of standard telecom fiber was implemented. The proposed approaches comprise a promising solution for construction of a high key rate and low-cost MDI-QKD network in the scenarios of access network or local area network, for instance, a central business district (CBD) of a city. It also provides a feasible technical reference for the possible metropolitan CV-MDI-QKD network. Furthermore, the developed technology of CV Bell detection of two remote independent quantum states will be an essential unit of CV quantum repeaters [55–57] in future wide-area quantum communication and the quantum Internet.

In our proof-of-principle experiment, relatively low repetition rates with light pulse widths of 50 ns are employed. To compensate for the frequency difference of the two independent lasers, the OPLL is adopted. Note that if a narrower pulse width is employed, such as 1 ns, it is unnecessary to actively lock the frequency difference of the two lasers. The frequency difference of current commercial frequency-stabilized semiconductor lasers can be readily stabilized to be less than several MHz level, and in this case, the relative phase variation will not change within 1 ns, so that the experimental implementation can be simplified.

The secure key rate and transmission distance can be significantly boosted by increasing the repetition rate and detection efficiency. By improving both the detection efficiency and reconciliation efficiency to 98%, the pulse repetition rate to 1 GHz [58], and suppressing the excess noise down to 0.002, CV-MDI-QKD can yield a secure key rate of 293 Mbps over 10 km of standard telecom fiber in the finite-size regime. Furthermore, by improving reconciliation efficiency to 99%, suppressing the electronic noise to 0.003, the transmission distance can be extended to 28 km.

In our future work, we will increase the repetition rate of the system to the order of GHz, and optimize the system performance to suppress the excess noise level to 0.002 and the electronic noise to 0.003. An experiment considering the composable security under finite code length will be implemented. Furthermore, the technology of integrated photonic chips is a promising solution for building miniaturized transmitters for CV-MDI-QKD.

APPENDIX A: PHASE EVOLUTION ANALYSIS

In this part, we analyze the phase evolution of Alice's signal and reference pulses, and Bob's signal and LO pulses in detail, which is beneficial to understand the phase estimation and compensation methods. As shown in Fig. 5, the phase evolution of Alice's signal and reference pulses can be expressed as follows:

$$\begin{aligned} S_A^X &= \theta_{\mathrm{src}}^A + \theta_{\mathrm{mod}}^A + \theta_{\mathrm{DL}}^A + \theta_{\mathrm{ch}}^A + \theta_{ac}^C + \theta_{cd}^C, \\ S_A^P &= \theta_{\mathrm{src}}^A + \theta_{\mathrm{mod}}^A + \theta_{\mathrm{DL}}^A + \theta_{\mathrm{ch}}^A + \theta_{ac}^C + \theta_{ce}^C, \\ R_A &= \theta_{\mathrm{src}}^A + \theta_{\mathrm{ch}}^A + \theta_{\mathrm{DL1}}^C + \theta_{ab}^C, \end{aligned} \tag{A1}$$

where $S_A^X(S_A^P)$ represents the phase of Alice's signal pulse before BS_2 (BS_3), R_A represents the phase of Alice's phase-reference pulses at the input port of the optical hybrid, θ_{src}^A is the phase of Alice's laser, θ_{mod}^A is the modulation phase of Alice, θ_{DL}^A is the accumulated phase by Alice's delay fiber, θ_{ch}^A is the accumulated phase by the transmission fiber from Alice to Charlie, θ_{ac}^C is the accumulated phase from the input port of Charlie to BS_1 that couples the signal pulses of Alice and Bob, and θ_{cd}^C is the accumulated phase from BS_1 to BS_2. Other phases in Eq. (A1) have expressions similar to the above.

The phase evolution of Bob's signal and LO pulses can be expressed as follows:

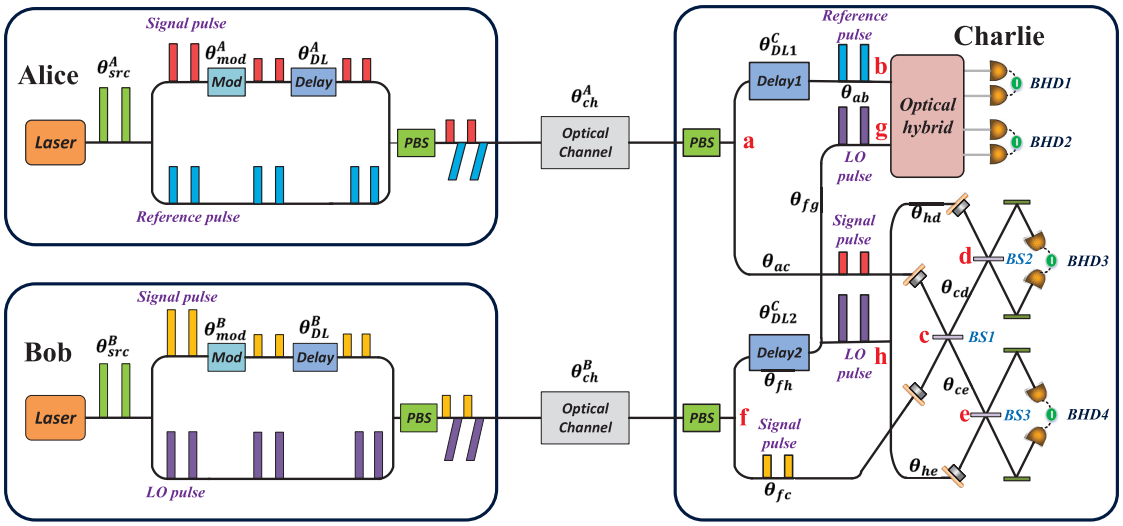

Fig. 5. Schematic of the phase evolution in CV-MDI-QKD.

$$
\begin{aligned}
S_B^X &= \theta_{\mathrm{src}}^B + \theta_{\mathrm{mod}}^B + \theta_{\mathrm{DL}}^B + \theta_{\mathrm{ch}}^B + \theta_{fc}^C + \theta_{cd}^C,\\
S_B^P &= \theta_{\mathrm{src}}^B + \theta_{\mathrm{mod}}^B + \theta_{\mathrm{DL}}^B + \theta_{\mathrm{ch}}^B + \theta_{fc}^C + \theta_{ce}^C,\\
L_B^X &= \theta_{\mathrm{src}}^B + \theta_{\mathrm{ch}}^B + \theta_{\mathrm{DL2}}^C + \theta_{fh}^C + \theta_{hd}^C,\\
L_B^P &= \theta_{\mathrm{src}}^B + \theta_{\mathrm{ch}}^B + \theta_{\mathrm{DL2}}^C + \theta_{fh}^C + \theta_{he}^C,\\
L_B^R &= \theta_{\mathrm{src}}^B + \theta_{\mathrm{ch}}^B + \theta_{\mathrm{DL2}}^C + \theta_{fg}^C,
\end{aligned}
\tag{A2}
$$

where $S_B^X(S_B^P)$ represents the phase of Bob's signal pulse before BS_2 (BS_3), $L_B^X(L_B^P)$ represents the phase of the LO pulse before BS_2 (BS_3), and L_B^R represents the phases of LO pulses at the input port of the optical hybrid. Note that the above optical phases will slowly fluctuate due to the influence of the external environment such as temperature and vibration.

The fast phase shift measured by the optical hybrid is given by

$$
\begin{aligned}
\Delta\theta &= L_B^R - R_A\\
&= (\theta_{\mathrm{src}}^B - \theta_{\mathrm{src}}^A) + (\theta_{\mathrm{ch}}^B - \theta_{\mathrm{ch}}^A) + (\theta_{\mathrm{DL2}}^C - \theta_{\mathrm{DL1}}^B) + (\theta_{fg}^C - \theta_{ab}^C).
\end{aligned}
\tag{A3}
$$

Thus, we have

$$
\begin{aligned}
L_B^X - S_A^X &= \Delta\theta + (\theta_{\mathrm{DL2}}^C - \theta_{\mathrm{DL}}^A) + (\theta_{fh}^C + \theta_{hd}^C - \theta_{ac}^C - \theta_{cd}^C)\\
&\quad - (\theta_{\mathrm{DL2}}^C - \theta_{\mathrm{DL1}}^B) - (\theta_{fg}^C - \theta_{ab}^C)\\
&= \Delta\theta + \varphi_A^X,\\
L_B^P - S_A^P &= \Delta\theta + (\theta_{\mathrm{DL2}}^C - \theta_{\mathrm{DL}}^A) + (\theta_{fh}^C + \theta_{he}^C - \theta_{ac}^C - \theta_{ce}^C)\\
&\quad - (\theta_{\mathrm{DL2}}^C - \theta_{\mathrm{DL1}}^B) - (\theta_{fg}^C - \theta_{ab}^C)\\
&= \Delta\theta + \varphi_A^P,\\
L_B^X - S_B^X &= (\theta_{\mathrm{DL2}}^C - \theta_{\mathrm{DL}}^B) + (\theta_{fh}^C + \theta_{hd}^C - \theta_{fc}^C - \theta_{cd}^C)\\
&= \varphi_B^X,\\
L_B^P - S_B^P &= (\theta_{\mathrm{DL2}}^C - \theta_{\mathrm{DL}}^B) + (\theta_{fh}^C + \theta_{he}^C - \theta_{fc}^C - \theta_{ce}^C)\\
&= \varphi_B^P.
\end{aligned}
\tag{A4}
$$

From Eq. (A4), we can see that the relative phase between Alice's signal pulses and LO pulses consists of two parts: the fast phase shift caused by independent lasers and transmission fiber links, and the slow phase drift accumulated by different optical paths. However, the relative phase between Bob's signal and LO pulses includes only the slow phase drift.

APPENDIX B: SLOW DRIFT PHASE ESTIMATION

From Eq. (A4), due to the existence of various phase shifts, the actual measurement results of the CV-BSM are

$$
\begin{aligned}
X_C &= \frac{1}{\sqrt{2}}\left[\left(X_A\cdot\cos\left(\Delta\theta+\varphi_A^X\right)+P_A\cdot\sin\left(\Delta\theta+\varphi_A^X\right)\right)\right.\\
&\quad\left.-\left(X_B\cdot\cos\varphi_B^X+P_B\cdot\sin\varphi_B^X\right)\right],\\
P_C &= \frac{1}{\sqrt{2}}\left[\left(X_A\cdot\cos\left(\Delta\theta+\varphi_A^P\right)+P_A\cdot\sin\left(\Delta\theta+\varphi_A^P\right)\right)\right.\\
&\quad\left.+\left(X_B\cdot\cos\varphi_B^P+P_B\cdot\sin\varphi_B^P\right)\right].
\end{aligned}
\tag{B1}
$$

For the slow phase drift, we use phase calibration pulses to accurately estimate the current phase in real time. We find that the fluctuation rate of the slow phase drift associated with variations of the optical lengths is of the order of Hertz, so that it can be considered as a constant within a frame time of $\Delta T = 10$ ms. There are 5000 pulses within one frame, and these pulses will be further divided into 50 data packets, whose patterns are shown in Supplement 1. In Bob's data packet, the first 24 pulses are phase calibration pulses divided into three groups with phases of $\theta_{\mathrm{mod}}^B \in \{0, 2\pi/3, 4\pi/3\}$. The amplitudes of the corresponding pulses in Alice's data packet are modulated to zero. The next 40 pulses are used as phase calibration pulses for Alice with phase $\theta_{\mathrm{mod}}^A = 0$ for the first 20 pulses and $\theta_{\mathrm{mod}}^A = \pi/2$ for the second 20 pulses. The amplitudes of the corresponding pulses in Bob's data packet are modulated to zero. Both Alice and Bob modulate the amplitude of the subsequent 16 pulses to zero for shot noise calibration. The last 20 pulses are employed as key pulses.

From Eq. (B1), the measurement results of Bob's phase calibration pulses are

$$X_C^{B,0} = -\frac{1}{\sqrt{2}} \cdot r_B \cdot \cos\varphi_B^X + x_N^1,$$
$$X_C^{B,2\pi/3} = -\frac{1}{\sqrt{2}} \left(-\frac{1}{2} \cdot r_B \cdot \cos\varphi_B^X + \frac{\sqrt{3}}{2} \cdot r_B \cdot \sin\varphi_B^X \right) + x_N^2,$$
$$X_C^{B,4\pi/3} = -\frac{1}{\sqrt{2}} \left(-\frac{1}{2} \cdot r_B \cdot \cos\varphi_B^X - \frac{\sqrt{3}}{2} \cdot r_B \cdot \sin\varphi_B^X \right) + x_N^3, \tag{B2}$$

$$P_C^{B,0} = \frac{1}{\sqrt{2}} \cdot r_B \cdot \cos\varphi_B^P + p_N^1,$$
$$P_C^{B,2\pi/3} = \frac{1}{\sqrt{2}} \left(-\frac{1}{2} \cdot r_B \cdot \cos\varphi_B^P + \frac{\sqrt{3}}{2} \cdot r_B \cdot \sin\varphi_B^P \right) + p_N^2,$$
$$P_C^{B,4\pi/3} = \frac{1}{\sqrt{2}} \left(-\frac{1}{2} \cdot r_B \cdot \cos\varphi_B^P - \frac{\sqrt{3}}{2} \cdot r_B \cdot \sin\varphi_B^P \right) + p_N^3, \tag{B3}$$

where r_B is the amplitude of the phase calibration pulses and x_N^j, p_N^j $(j = 1, 2, 3)$ denote vacuum fluctuation noises, which are independently and identically distributed Gaussian noises with zero mean. In our experiment, each phase calibration pulse includes around 90 photons; thus, a single phase calibration pulse cannot provide accurate phase estimation due to the influence of vacuum fluctuations. To eliminate the impact of vacuum noise and obtain an accurate estimated value, we average the measurement results of 400 of Bob's phase calibration pulses with the same modulation phase in each frame. We denote the average values of three types of phase calibration pulses as U_0^X, U_2^X, U_4^X, U_0^P, U_2^P, and U_4^P. In this case, slow phase drifts φ_B^X and φ_B^P can be estimated by

$$\tan(\varphi_B^X) = \frac{\sqrt{3}(U_4^X - U_2^X)}{2U_0^X - U_2^X - U_4^X},$$
$$\tan(\varphi_B^P) = \frac{\sqrt{3}(U_4^P - U_2^P)}{2U_0^P - U_2^P - U_4^P}. \tag{B4}$$

The measurement results of Alice's phase calibration pulses are given by

$$X_C^{A,0} = \frac{1}{\sqrt{2}} \cdot r_A \cdot \cos(\Delta\theta_1 + \varphi_A^X) + x_N^4,$$
$$X_C^{A,\frac{\pi}{2}} = \frac{1}{\sqrt{2}} \cdot r_A \cdot \sin(\Delta\theta_2 + \varphi_A^X) + x_N^5, \tag{B5}$$
$$P_C^{A,0} = \frac{1}{\sqrt{2}} \cdot r_A \cdot \cos(\Delta\theta_1 + \varphi_A^P) + p_N^4,$$
$$P_C^{A,\frac{\pi}{2}} = \frac{1}{\sqrt{2}} \cdot r_A \cdot \sin(\Delta\theta_2 + \varphi_A^P) + p_N^5, \tag{B6}$$

where r_A is the amplitude of the phase calibration pulses, and $\Delta\theta_1$, $\Delta\theta_2$ are fast phase shifts measured by the optical hybrid, which are known in the estimation process of the slow phase drift. x_N^j, p_N^j $(j = 4, 5)$ denote vacuum fluctuation noises. Because the fast phase shift of each phase calibration pulse is random, the impact of vacuum noise cannot be eliminated by simply averaging a large number of measurement results of Alice's phase calibration pulses with the same modulation phase.

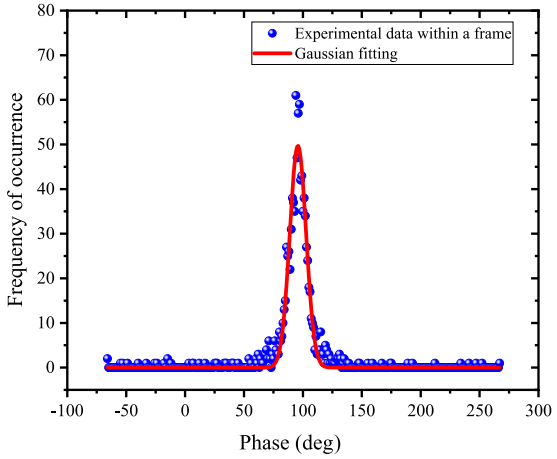

Fig. 6. Statistics distribution diagram obtained with the results of Alice's phase calibration pulses in one frame. Blue dots are experimental results derived from 1000 pairs of phase calibration pulses. The red solid curve denotes Gaussian fitting of experimental data.

To estimate φ_A^X and φ_A^P, we propose a feasible estimation method that can be obtained by two phase calibration pulses modulated with phases zero and $\pi/2$:

$$\tan(\varphi_A^X) \approx \frac{X_C^{A,\frac{\pi}{2}} \cdot \cos(\Delta\theta_1) - X_C^{A,0} \cdot \sin(\Delta\theta_2)}{X_C^{A,0} \cdot \cos(\Delta\theta_2) + X_C^{A,\frac{\pi}{2}} \cdot \sin(\Delta\theta_1)},$$
$$\tan(\varphi_A^P) \approx \frac{P_C^{A,\frac{\pi}{2}} \cdot \cos(\Delta\theta_1) - P_C^{A,0} \cdot \sin(\Delta\theta_2)}{P_C^{A,0} \cdot \cos(\Delta\theta_2) + P_C^{A,\frac{\pi}{2}} \cdot \sin(\Delta\theta_1)}. \tag{B7}$$

In this way, we can get 1000 phase estimate values in each frame. By making a probability statistics and Gaussian fitting on the estimated values, the phase values corresponding to the maximum probability distribution are extracted and regarded as the estimated values of slow phase drifts φ_A^X and φ_A^P. Since the vacuum noises are Gaussian noises with zero mean, the maximum probability distribution is zero, and the impact of vacuum noise can be eliminated. Figure 6 shows a typical statistics distribution diagram of φ_A^X obtained in terms of the measured phase calibration pulses in one frame.

APPENDIX C: CLOCK SYNCHRONIZATION

In the case of no long-distance transmission fibers being connected, we select the appropriate length of delay fibers at the sites of Alice, Bob, and Charlie, so that the signal and reference pulses of Alice, and the signal and LO pulses of Bob arrive at the four BHDs at the same time. When Alice and Bob are connected to long-distance transmission fibers of different lengths, they select the appropriate delay through their pulse generators, so that the delay within one repetition period can be compensated for. For example, the distance between Bob and Charlie is shorter than that of Alice and Charlie, so Bob's signal pulses will arrive at Charlie's

site first. In this case, we discard those early arrival signal pulses from Bob until the first signal pulse of Alice arrives.

At Charlie's site, a portion of the LO pulses after polarization-de-multiplexing is detected by a photodetector, and the output electrical pulses are input into a homemade clock recovery module to obtain an amplified sync signal with adjustable delay. By finely adjusting the delay, the peak value of each output electrical pulse of the time-domain BHDs can be sampled by the data acquisition card to yield a single value of the signal (reference) field quadrature.

When considering an actual field CV-MDI-QKD, the solution demonstrated in [39] can be used. The basic procedure is as follows: Charlie sends synchronized laser-pulse trains to Alice and Bob to synchronize the laser pulses of Alice and Bob and Charlie's local clock. The measured arrival times at Charlie's site are used as a feedback signal to adjust the relative delay between the synchronization laser-pulse trains of Alice and Bob, to ensure that the arrival times of Alice and Bob's laser pulses are the same.

Funding. National Key Research and Development Program of China (2016YFA0301403); National Natural Science Foundation of China (62175138); Key Research and Development Program of Guangdong Province (2020B0303040002); Shanxi 1331KSC.

Disclosures. The authors declare no conflicts of interests.

Data availability. Datasets generated and analyzed for simulation are available from the corresponding author upon reasonable request.

Supplemental document. See Supplement 1 for supporting content.

REFERENCES

1. N. Gisin, G. Ribordy, W. Tittel, and H. Zbinden, "Quantum cryptography," Rev. Mod. Phys. **74**, 145–195 (2002).
2. V. Scarani, H. Bechmann-Pasquinucci, N. J. Cerf, M. Dušek, N. Lütkenhaus, and M. Peev, "The security of practical quantum key distribution," Rev. Mod. Phys. **81**, 1301–1350 (2009).
3. H.-K. Lo, M. Curty, and K. Tamaki, "Secure quantum key distribution," Nat. Photonics **8**, 595–604 (2014).
4. E. Diamanti, H.-K. Lo, B. Qi, and Z. Yuan, "Practical challenges in quantum key distribution," npj Quantum Inf. **2**, 16025 (2016).
5. S. Pirandola, U. L. Andersen, L. Banchi, M. Berta, D. Bunandar, R. Colbeck, D. Englund, T. Gehring, C. Lupo, C. Ottaviani, J. L. Pereira, M. Razavi, J. S. Shaari, M. Tomamichel, V. C. Usenko, G. Vallone, P. Villoresi, and P. Wallden, "Advances in quantum cryptography," Adv. Opt. Photon. **12**, 1012–1236 (2020).
6. F. Xu, X. Ma, Q. Zhang, H.-K. Lo, and J.-W. Pan, "Secure quantum key distribution with realistic devices," Rev. Mod. Phys. **92**, 025002 (2020).
7. H.-K. Lo, M. Curty, and B. Qi, "Measurement-device-independent quantum key distribution," Phys. Rev. Lett. **108**, 130503 (2012).
8. S. L. Braunstein and S. Pirandola, "Side-channel-free quantum key distribution," Phys. Rev. Lett. **108**, 130502 (2012).
9. S. L. Braunstein and P. van Loock, "Quantum information with continuous variables," Rev. Mod. Phys. **77**, 513–577 (2005).
10. C. Weedbrook, S. Pirandola, R. Garca-Patrón, N. J. Cerf, T. C. Ralph, J. H. Shapiro, and S. Lloyd, "Gaussian quantum information," Rev. Mod. Phys. **84**, 621–669 (2012).
11. T. C. Ralph, "Continuous variable quantum cryptography," Phys. Rev. A **61**, 010303 (1999).
12. F. Grosshans, G. Van Assche, J. Wenger, R. Brouri, N. J. Cerf, and P. Grangier, "Quantum key distribution using Gaussian-modulated coherent states," Nature **421**, 238–241 (2003).
13. S. Pirandola, R. Laurenza, C. Ottaviani, and L. Banchi, "Fundamental limits of repeaterless quantum communications," Nat. Commun. **8**, 15043 (2017).
14. B. Qi, W. Zhu, L. Qian, and H.-K. Lo, "Feasibility of quantum key distribution through a dense wavelength division multiplexing network," New J. Phys. **12**, 103042 (2010).
15. R. Kumar, H. Qin, and R. Alléaume, "Coexistence of continuous variable QKD with intense DWDM classical channels," New J. Phys. **17**, 043027 (2015).
16. N. Wang, S. Du, W. Liu, X. Wang, Y. Li, and K. Peng, "Long-distance continuous-variable quantum key distribution with entangled states," Phys. Rev. Appl. **10**, 064028 (2018).
17. X.-C. Ma, S.-H. Sun, M.-S. Jiang, and L.-M. Liang, "Wavelength attack on practical continuous-variable quantum-key-distribution system with a heterodyne protocol," Phys. Rev. A **87**, 052309 (2013).
18. J.-Z. Huang, S. Kunz-Jacques, P. Jouguet, C. Weedbrook, Z.-Q. Yin, S. Wang, W. Chen, G.-C. Guo, and Z.-F. Han, "Quantum hacking on quantum key distribution using homodyne detection," Phys. Rev. A **89**, 032304 (2014).
19. P. Jouguet, S. Kunz-Jacques, and E. Diamanti, "Preventing calibration attacks on the local oscillator in continuous-variable quantum key distribution," Phys. Rev. A **87**, 062313 (2013).
20. H. Qin, R. Kumar, and R. Alléaume, "Quantum hacking: saturation attack on practical continuous-variable quantum key distribution," Phys. Rev. A **94**, 012325 (2016).
21. X. Ma, C.-H. F. Fung, and M. Razavi, "Statistical fluctuation analysis for measurement-device-independent quantum key distribution," Phys. Rev. A **86**, 052305 (2012).
22. X.-B. Wang, "Three-intensity decoy-state method for device-independent quantum key distribution with basis-dependent errors," Phys. Rev. A **87**, 012320 (2013).
23. M. Curty, F. Xu, W. Cui, C. C. W. Lim, K. Tamaki, and H.-K. Lo, "Finite-key analysis for measurement-device-independent quantum key distribution," Nat. Commun. **5**, 3732 (2014).
24. F. Xu, H. Xu, and H.-K. Lo, "Protocol choice and parameter optimization in decoy-state measurement-device-independent quantum key distribution," Phys. Rev. A **89**, 052333 (2014).
25. Y.-H. Zhou, Z.-W. Yu, and X.-B. Wang, "Making the decoy-state measurement-device-independent quantum key distribution practically useful," Phys. Rev. A **93**, 042324 (2016).
26. A. Rubenok, J. A. Slater, P. Chan, I. Lucio-Martinez, and W. Tittel, "Real-world two-photon interference and proof-of-principle quantum key distribution immune to detector attacks," Phys. Rev. Lett. **111**, 130501 (2013).
27. Y. Liu, T.-Y. Chen, L.-J. Wang, H. Liang, G.-L. Shentu, J. Wang, K. Cui, H.-L. Yin, N.-L. Liu, L. Li, X. Ma, J. S. Pelc, M. M. Fejer, C.-Z. Peng, Q. Zhang, and J.-W. Pan, "Experimental measurement-device-independent quantum key distribution," Phys. Rev. Lett. **111**, 130502 (2013).
28. Z. Tang, Z. Liao, F. Xu, B. Qi, L. Qian, and H.-K. Lo, "Experimental demonstration of polarization encoding measurement-device-independent quantum key distribution," Phys. Rev. Lett. **112**, 190503 (2014).
29. L. C. Comandar, M. Lucamarini, B. Frohlich, J. F. Dynes, A. W. Sharpe, S. W.-B. Tam, Z. L. Yuan, R. V. Penty, and A. J. Shields, "Quantum key distribution without detector vulnerabilities using optically seeded lasers," Nat. Photonics **10**, 312–315 (2016).
30. H.-L. Yin, T.-Y. Chen, Z.-W. Yu, H. Liu, L.-X. You, Y.-H. Zhou, S.-J. Chen, Y. Mao, M.-Q. Huang, W.-J. Zhang, H. Chen, M. J. Li, D. Nolan, F. Zhou, X. Jiang, Z. Wang, Q. Zhang, X.-B. Wang, and J.-W. Pan, "Measurement-device-independent quantum key distribution over a 404 km optical fiber," Phys. Rev. Lett. **117**, 190501 (2016).
31. Y. Cao, Y.-H. Li, K.-X. Yang, Y.-F. Jiang, S.-L. Li, X.-L. Hu, M. Abulizi, C.-L. Li, W. Zhang, Q.-C. Sun, W.-Y. Liu, X. Jiang, S.-K. Liao, J.-G. Ren, H. Li, L. You, Z. Wang, J. Yin, C.-Y. Lu, X.-B. Wang, Q. Zhang, C.-Z. Peng, and J.-W. Pan, "Long-distance free-space measurement-device-independent quantum key distribution," Phys. Rev. Lett. **125**, 260503 (2020).
32. X.-B. Wang, Z.-W. Yu, and X.-L. Hu, "Twin-field quantum key distribution with large misalignment error," Phys. Rev. A **98**, 062323 (2018).
33. M. Minder, M. Pittaluga, G. L. Roberts, M. Lucamarini, J. F. Dynes, Z. L. Yuan, and A. J. Shields, "Experimental quantum key distribution beyond the repeaterless secret key capacity," Nat. Photonics **13**, 334–338 (2019).
34. Y. Liu, Z.-W. Yu, W. Zhang, J.-Y. Guan, J.-P. Chen, C. Zhang, X.-L. Hu, H. Li, C. Jiang, J. Lin, T.-Y. Chen, L. You, Z. Wang, X.-B. Wang, Q. Zhang, and J.-W. Pan, "Experimental twin-field quantum key distribution through sending or not sending," Phys. Rev. Lett. **123**, 100505 (2019).
35. S. Wang, D.-Y. He, Z.-Q. Yin, F.-Y. Lu, C.-H. Cui, W. Chen, Z. Zhou, G.-C. Guo, and Z.-F. Han, "Beating the fundamental rate-distance limit in a proof-of-principle quantum key distribution system," Phys. Rev. X **9**, 021046 (2019).

36. X. Zhong, J. Hu, M. Curty, L. Qian, and H.-K. Lo, "Proof-of-principle experimental demonstration of twin-field type quantum key distribution," Phys. Rev. Lett. **123**, 100506 (2019).
37. J.-P. Chen, C. Zhang, Y. Liu, C. Jiang, W. Zhang, X.-L. Hu, J.-Y. Guan, Z.-W. Yu, H. Xu, J. Lin, M.-J. Li, H. Chen, H. Li, L. You, Z. Wang, X.-B. Wang, Q. Zhang, and J.-W. Pan, "Sending-or-not-sending with independent lasers: secure twin-field quantum key distribution over 509 km," Phys. Rev. Lett. **124**, 070501 (2020).
38. X.-T. Fang, P. Zeng, H. Liu, M. Zou, W. Wu, Y.-L. Tang, Y.-J. Sheng, Y. Xiang, W. Zhang, H. Li, Z. Wang, L. You, M.-J. Li, H. Chen, Y.-A. Chen, Q. Zhang, C.-Z. Peng, X. Ma, T.-Y. Chen, and J.-W. Pan, "Implementation of quantum key distribution surpassing the linear rate-transmittance bound," Nat. Photonics **14**, 422–425 (2020).
39. J.-P. Chen, C. Zhang, Y. Liu, C. Jiang, W.-J. Zhang, Z.-Y. Han, S.-Z. Ma, X.-L. Hu, Y.-H. Li, H. Liu, F. Zhou, H.-F. Jiang, T.-Y. Chen, H. Li, L.-X. You, Z. Wang, X.-B. Wang, Q. Zhang, and J.-W. Pan, "Twin-field quantum key distribution over a 511 km optical fibre linking two distant metropolitan areas," Nat. Photonics **15**, 570–575 (2021).
40. S. Pirandola, C. Ottaviani, G. Spedalieri, C. Weedbrook, S. L. Braunstein, S. Lloyd, T. Gehring, C. S. Jacobsen, and U. L. Andersen, "High-rate measurement-device-independent quantum cryptography," Nat. Photonics **9**, 397–402 (2015).
41. Z. Li, Y.-C. Zhang, F. Xu, X. Peng, and H. Guo, "Continuous-variable measurement-device-independent quantum key distribution," Phys. Rev. A **89**, 052301 (2014).
42. X.-C. Ma, S.-H. Sun, M.-S. Jiang, M. Gui, and L.-M. Liang, "Gaussian-modulated coherent-state measurement-device-independent quantum key distribution," Phys. Rev. A **89**, 042335 (2014).
43. P. Papanastasiou, C. Ottaviani, and S. Pirandola, "Finite-size analysis of measurement-device-independent quantum cryptography with continuous variables," Phys. Rev. A **96**, 042332 (2017).
44. X. Zhang, Y. Zhang, Y. Zhao, X. Wang, S. Yu, and H. Guo, "Finite-size analysis of continuous-variable measurement-device-independent quantum key distribution," Phys. Rev. A **96**, 042334 (2017).
45. C. Lupo, C. Ottaviani, P. Papanastasiou, and S. Pirandola, "Continuous-variable measurement-device-independent quantum key distribution: composable security against coherent attacks," Phys. Rev. A **97**, 052327 (2018).
46. Z. Chen, Y. Zhang, G. Wang, Z. Li, and H. Guo, "Composable security analysis of continuous-variable measurement-device-independent quantum key distribution with squeezed states for coherent attacks," Phys. Rev. A **98**, 012314 (2018).
47. P. Wang, X. Wang, and Y. Li, "Continuous-variable measurement-device-independent quantum key distribution using modulated squeezed states and optical amplifiers," Phys. Rev. A **99**, 042309 (2019).
48. H.-X. Ma, P. Huang, D.-Y. Bai, T. Wang, S.-Y. Wang, W.-S. Bao, and G.-H. Zeng, "Long-distance continuous-variable measurement-device-independent quantum key distribution with discrete modulation," Phys. Rev. A **99**, 022322 (2019).
49. K. N. Wilkinson, P. Papanastasiou, C. Ottaviani, T. Gehring, and S. Pirandola, "Long-distance continuous-variable measurement-device-independent quantum key distribution with postselection," Phys. Rev. Res. **2**, 033424 (2020).
50. B. Qi, P. Lougovski, R. Pooser, W. Grice, and M. Bobrek, "Generating the local oscillator "locally" in continuous-variable quantum key distribution based on coherent detection," Phys. Rev. X **5**, 041009 (2015).
51. D. B. S. Soh, C. Brif, P. J. Coles, N. Lütkenhaus, R. M. Camacho, J. Urayama, and M. Sarovar, "Self-referenced continuous-variable quantum key distribution protocol," Phys. Rev. X **5**, 041010 (2015).
52. X. Wang, W. Liu, P. Wang, and Y. Li, "Experimental study on all-fiber-based unidimensional continuous-variable quantum key distribution," Phys. Rev. A **95**, 062330 (2017).
53. C. Lupo, C. Ottaviani, P. Papanastasiou, and S. Pirandola, "Parameter estimation with almost no public communication for continuous-variable quantum key distribution," Phys. Rev. Lett. **120**, 220505 (2018).
54. S. Pirandola, C. Ottaviani, G. Spedalieri, C. Weedbrook, S. L. Braunstein, S. Lloyd, T. Gehring, C. S. Jacobsen, and U. L. Andersen, "Reply to 'discrete and continuous variables for measurement-device-independent quantum cryptography'," Nat. Photonics **9**, 773–775 (2015).
55. J. Dias and T. C. Ralph, "Quantum repeaters using continuous-variable teleportation," Phys. Rev. A **95**, 022312 (2017).
56. F. Furrer and W. J. Munro, "Repeaters for continuous-variable quantum communication," Phys. Rev. A **98**, 032335 (2018).
57. K. P. Seshadreesan, H. Krovi, and S. Guha, "Continuous-variable quantum repeater based on quantum scissors and mode multiplexing," Phys. Rev. Res. **2**, 013310 (2020).
58. Z. Qu, I. B. Djordjevic, and M. A. Neifeld, "RF-subcarrier-assisted four-state continuous-variable QKD based on coherent detection," Opt. Lett. **41**, 5507–5510 (2016).